CHARACTERIZING THE COOL KOIs. II. THE M DWARF KOI-254 AND ITS HOT JUPITER*

John Asher Johnson[1,2], J. Zachary Gazak[3], Kevin Apps[4], Philip S. Muirhead[1], Justin R. Crepp[1], Ian J. M. Crossfield[5],
Tabetha Boyajian[6,11], Kaspar von Braun[2], Barbara Rojas-Ayala[7], Andrew W. Howard[8], Kevin R. Covey[9,11],
Everett Schlawin[9], Katherine Hamren[10], Timothy D. Morton[1], Geoffrey W. Marcy[8], and James P. Lloyd[9]

[1] Department of Astrophysics, California Institute of Technology, MC 249-17, Pasadena, CA 91125, USA; johnjohn@astro.caltech.edu
[2] NASA Exoplanet Science Institute (NExScI), CIT Mail Code 100-22, 770 South Wilson Avenue, Pasadena, CA 91125, USA
[3] Institute for Astronomy, University of Hawai'i, 2680 Woodlawn Drive, Honolulu, HI 96822, USA
[4] Cheyne Walk Observatory, 75B Cheyne Walk, Horley, Surrey, RH6 7LR, UK
[5] Department of Physics and Astronomy, University of California Los Angeles, Los Angeles, CA 90095, USA
[6] Center for High Angular Resolution Astronomy and Department of Physics and Astronomy, Georgia State University,
P.O. Box 4106, Atlanta, GA 30302-4106, USA
[7] Department of Astrophysics, Division of Physical Sciences, American Museum of Natural History, Central Park West at 79th Street, New York, NY 10024, USA
[8] Department of Astronomy, University of California, Mail Code 3411, Berkeley, CA 94720, USA
[9] Department of Astronomy, Cornell University, Ithaca, NY 14853, USA
[10] Department of Astronomy and Astrophysics, University of California, Santa Cruz, CA 95064, USA

ABSTRACT

We report the confirmation and characterization of a transiting gas giant planet orbiting the M dwarf KOI-254 every 2.455239 days, which was originally discovered by the *Kepler* mission. We use radial velocity measurements, adaptive optics imaging, and near-infrared spectroscopy to confirm the planetary nature of the transit events. KOI-254 b is the first hot Jupiter discovered around an M-type dwarf star. We also present a new model-independent method of using broadband photometry to estimate the mass and metallicity of an M dwarf without relying on a direct distance measurement. Included in this methodology is a new photometric metallicity calibration based on $J - K$ colors. We use this technique to measure the physical properties of KOI-254 and its planet. We measure a planet mass of $M_P = 0.505\,M_{\rm Jup}$, radius $R_P = 0.96\,R_{\rm Jup}$, and semimajor axis $a = 0.030$ AU, based on our measured stellar mass $M_\star = 0.59\,M_\odot$ and radius $R_\star = 0.55\,R_\odot$. We also find that the host star is metal-rich, which is consistent with the sample of M-type stars known to harbor giant planets.

Key words: planetary systems – techniques: photometric – techniques: radial velocities – techniques: spectroscopic

Online-only material: color figures

1. INTRODUCTION

Of the hundreds of planets discovered outside of the solar system the class known as hot Jupiters, with periods $P < 10$ days and $M_P \gtrsim 0.2\,M_{\rm Jup}$, has provided much of our knowledge about the internal structures and compositions of exoplanets (Charbonneau et al. 2007; Winn 2008). The crucial role hot Jupiters play in present-day exoplanetary science is not because they are common; the occurrence rate of hot Jupiters in the solar neighborhood is only about 1% (Marcy et al. 2005). Rather, close-in giant planets are the most easily detectable variety for Doppler and transit surveys owing to the large reflex motions and transit depths they induce. Once found to transit their host stars, their relatively large atmospheric cross-sections make them favorable targets for various follow-up studies to measure planet properties such as atmospheric composition, atmospheric temperature profiles, phase curves, and spin-orbit angles (e.g., Knutson et al. 2009; Crossfield et al. 2010; Madhusudhan & Seager 2011; Albrecht et al. 2011).

While only one in every hundred Sun-like stars harbors a close-in gas giant planet, the occurrence of hot Jupiters is even further depressed around the Galaxy's most numerous denizens, the M dwarfs. This empirical finding has emerged from various Doppler surveys of M dwarfs, which have detected zero close-in giant planets among roughly 300 target stars with masses $M_\star < 0.6\,M_\odot$, despite the ready detectability of the large Doppler amplitudes of these short-period giants (Endl et al. 2003; Johnson et al. 2010a). This lack of hot Jupiters around M dwarfs, as well as the overall dearth of giant planets around low-mass stars, is likely due to the inefficiency of the planet-formation process within low-mass protoplanetary disks (Laughlin et al. 2004; Ida & Lin 2005; Kennedy & Kenyon 2008). This notion is further bolstered by the elevated occurrence of giant planets around stars more massive than the Sun (Johnson et al. 2007, 2010a).

To date, no planet more massive than $0.1\,M_{\rm Jup}$ has been discovered around an M dwarf with a period less than 30 days.[12] However, orbital companions at either mass extreme have been detected around M dwarfs, and some have been found to transit their stars. At the high-mass end, two transiting brown dwarfs have been found by the *MEarth* and *Kepler* transit surveys, respectively (Irwin et al. 2010; Johnson et al. 2011a). At the other end of the mass scale, transits of the radial velocity (RV)-detected, short-period Neptune Gl 436 b were detected by ground-based follow-up photometry (Butler et al. 2004; Gillon et al. 2007), and the *MEarth* survey discovered a transiting super earth orbiting the nearby, low-mass star GJ 1214 (Charbonneau et al. 2009). However, no close-in planet with a mass intermediate to those previous discoveries has been found

[12] http://exoplanets.org
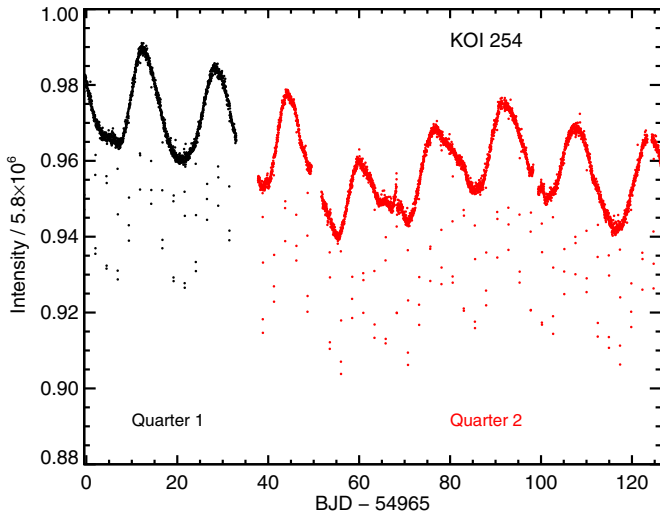
Figure 1. Normalized *Kepler* photometry vs. time showing the rotational modulation of star spots, from which we derive a rotation period.

(A color version of this figure is available in the online journal.)

Table 1
Observed Properties of KOI-254

Parameter	Value	Adopted Uncertainty	Source
α	19 31 29.50	...	KIC
δ	+41 03 51.4	...	KIC
μ_α (mas yr^{-1})	6	...	KIC
μ_δ (mas yr^{-1})	−20	...	KIC
g	17.41 ± 0.02	...	KIC
r	16.11 ± 0.02	...	KIC
i	13.364 ± 0.02	...	KIC
z	15.001 ± 0.02	...	KIC
K_P[a]	15.979 ± 0.03	...	KIC
V	16.88 ± 0.05	0.11	KIC[b]
J	13.75 ± 0.024	0.22	2MASS
H	13.08 ± 0.025	0.20	2MASS
K_S	12.89 ± 0.030	0.18	2MASS

Notes.
[a] *Kepler*-band magnitude.
[b] *V*-band magnitude converted from *r* magnitude.

around an M dwarf. This leaves a gap in the companion-mass continuum that spans more than two orders of magnitude, from $0.1\ M_{\rm Jup}$ to 30 $M_{\rm Jup}$.

One of the planet candidates discovered by the *Kepler* mission, KOI-254.01, provides an opportunity to fill in this missing region of parameter space. Borucki et al. (2011) reported a transit depth of $\delta = 3.9093\%$ and a period of $P = 2.455239$ days for the planet candidate. The large transit depth and lack of a visible secondary eclipse, together with the lack of a pixel shift in the stellar position during transit, reduces the a priori probability that the transit is a false-positive to 1.9% (Morton & Johnson 2011). However, it is nonetheless desirable and prudent to acquire a full suite of follow-up observations to rule out a false positive. We also characterize the stellar characteristics of the low-mass host star in order to accurately and precisely measure the properties of the planet.

This contribution thus builds on the work of Muirhead et al. (2011), hereafter Paper 1, who presented a spectroscopic analysis of all of the M dwarf KOIs announced by Borucki et al. (2011). We add to that work by including additional data from our multi-band, multi-site follow-up campaign for the specific case of the KOI-254 planetary system. In Section 2 we present our observations of KOI-254. In Section 3 we describe our analysis of the *Kepler* light curves, KIC photometry, infrared spectra, and RV orbit. We describe our results in Section 4 and conclude with a brief discussion and summary in Section 5.

2. OBSERVATIONS

2.1. Kepler Photometry

The *Kepler* Object of Interest KOI-254 (=KIC 5794240, =2MASS 19312949+4103513) is identified in the *Kepler* Input Catalog (KIC; Batalha et al. 2010; Brown et al. 2011) as a cool dwarf star with $T_{\rm eff} = 3948$ K and $\log g = 4.54$ and a *Kepler* magnitude $K_P = 15.98$ (no errors are reported). Periodic, deep transit events were detected and reported by Borucki et al. (2011), with a period $P = 2.455239 \pm 0.000004$ days and a depth of 3.9093%.

KOI-254 was not observed during the Q0 observing quarter, but was during subsequent quarters. We downloaded the Q1 and Q2 data sets from the NASA Multimission Archive at STScI

(MAST). The photometric measurements span from 2009 May 13 to 2009 September 16 and have a 29.4244 minute cadence and a median fractional uncertainty of 6×10^{-4}. In addition to the transit events, KOI-254's *Kepler* light curve shows a clear 14 day periodicity, with a coherent 3% modulation persisting over the full 122 day baseline. This additional variability is most likely due to rotational modulation of star spots, which is useful for setting limits on the system age (Section 4.3).

The KIC lists additional photometric data in the Sloan Digital Sky Survey (SDSS) bands, as well as near-infrared (NIR) photometry from the Two-Micron All-Sky Survey (2MASS; Skrutskie et al. 2006), which we reproduce in Table 1.

2.2. Nickel Z-band Photometry

To check for achromatic transit depths and to update the ephemeris over that provided by Q2 data, we observed the transit predicted to occur on UT 2011 June 30 using the 1 m Nickel telescope at Lick Observatory on Mt. Hamilton, California. We used the Nickel Direct Imaging Camera, which comprises a thinned Loral 2048^2-pixel CCD with a 6′.3 square field of view (e.g., Johnson et al. 2008). We observed through a Gunn Z filter, used 2×2 binning for an effective pixel scale of 0′′37 pixel^{-1}, and a constant exposure time of 120 s. We used the fast readout mode, with approximately 13 s between exposures to read the full frame and reset the detector.

The conditions were clear, and the seeing and telescope optics delivered a full width at half maximum of $\sim$1′′5. We began observing as soon as possible after sunset at an air mass of 1.55 and observed continuously for 7.4 hr bracketing the predicted transit midpoint, ending at an air mass of 1.21. Guiding was unsteady for the first 1.5 hr but settled down thereafter, subsequently needing only small occasional adjustments to keep the stars as nearly as possible on the same pixels.

We measured the instrumental magnitude of KOI-254 with respect to four nearby stars with KIC numbers 5794268, 5794279, 5794302, and 5794355. An aperture width of 22 pixels (with a sky annulus of inner and outer diameter of 27 and 32 pixels, respectively) gave the lowest out-of-transit photometric scatter. The Nickel dome partially occults the telescope when observing within 5.7 degrees of zenith; this introduced systematic photometric variations that caused us to
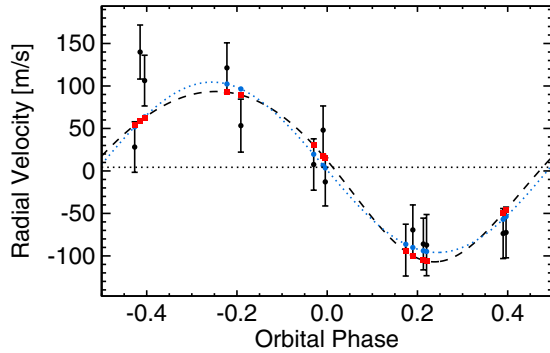
Figure 2. Keck/HIRES radial velocity measurements of KOI-254 (black with error bars) phased to the transit-based orbital period. The error bars represent the quadrature sum of the internal measurement errors and 23 m s^{-1} of additional instrumental noise based on our analysis of low signal-to-noise measurements of a stable M dwarf. The dashed line shows the best-fitting Keplerian model, and the red squares are the model evaluated at the times of measurement.

(A color version of this figure is available in the online journal.)

excise 40 minutes of observations, including the transit egress. We converted the Nickel timestamps to BJD$_{UTC}$ using the techniques of Eastman et al. (2010) to be consistent with the *Kepler* data.

2.3. Keck/HIRES Velocimetry

We obtained spectroscopic observations of KOI-254 at Keck Observatory using the High Resolution Echelle Spectrometer (HIRES) with the standard iodine-cell setup used by the California Planet Survey (Howard et al. 2010). Because of the star's faintness ($V = 16.88$) we used the C2 decker corresponding to a projected size of $14\farcs0 \times 0\farcs851$ to allow sky subtraction and a resolving power of $R = \lambda/\Delta\lambda \approx 55,000$. We obtained 14 observations of KOI-254, all with an exposure time of 1200 s, resulting in a signal-to-noise ratio (S/N) of 13–16 at 5500 Å.

We used the Butler et al. (1996) iodine cell method to measure the RV time series of KOI-254 with respect to an iodine-free "template" observation that has had its instrumental profile removed through deconvolution. However, since KOI-254 is so faint, obtaining a high-S/N, high-resolution template would be prohibitively expensive in observing time. We instead selected a surrogate star with the same spectral type as KOI-254 (HD 199305, M0V) and adjusted the line depths and widths using the "spectral morphing" technique of Johnson et al. (2006). We then used this morphed, deconvolved template in our RV analysis.

To ensure that our Doppler analysis pipeline produced reliable RV measurements, we obtained a sequence of test exposures of the M0V star HIP 36834, which has demonstrated RVs stable at the 5.3 m s^{-1} level over the past seven years at Keck. Our test exposures were made at S/N = 15 and a morphed template based on the same surrogate stellar spectrum used for KOI-254. We find a root mean square (rms) of 23 m s^{-1} during a time span of 20 days. We adopt this rms as our RV measurement uncertainty for KOI-254.

Figure 2 shows our 14 RV measurements of KOI-254 phased at the transit period, with the error bars corresponding to our estimated 23 m s^{-1} measurement precision. The best-fitting Keplerian model is shown as a dashed line and described in Section 3. The RV measurements, HJD times of observation and internal uncertainties are listed in Table 2.
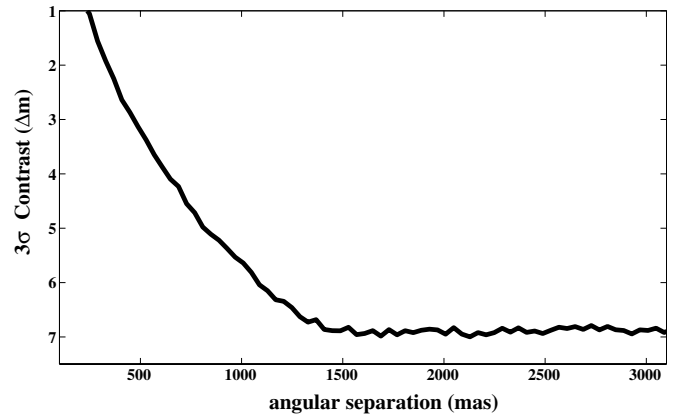
Figure 3. Contrast limits based on the high spatial resolution K' image of KOI 254 taken with NIRC2 and the Keck AO system on 2011 June 24 UT. The contrast is measured in magnitudes with respect to the central star. The AO observations probe regions interior to the *Kepler* photometric aperture and help to eliminate candidate false-positive signals at brightness levels comparable to the transit depth. No nearby stars were detected.

Table 2
Radial Velocities for KOI254

HJD −2440000	RV (m s^{-1})	Uncertainty[a] (m s^{-1})
15671.1050	53.33	18.62
15672.0980	−86.01	17.40
15673.0120	139.94	19.69
15674.0079	48.02	13.62
15700.9641	7.57	16.95
15703.9588	−69.43	15.50
15705.9376	−12.86	13.37
15706.9214	−72.40	16.29
15727.0516	106.32	16.34
15731.0411	−87.29	25.96
15733.9132	−73.68	15.64
15734.8653	121.33	15.54
15735.8384	−93.17	17.49
15763.8262	28.13	16.09

Notes. [a] Uncertainties represent formal measurement uncertainties and do not include the 23 m s^{-1} instrumental systematics we include in our orbit analysis.

2.4. Keck Adaptive Optics Imaging

We obtained adaptive optics (AO) images of KOI-254 on 2011 June 24 UT using the NIRC2 camera at Keck II, in order to reduce the likelihood for false positives by searching for any sources that could mimic a planetary transit signal, such as a nearby eclipsing binary. With $r = 16.11$ mag, KOI-254 is relatively faint for natural guide star observations. Nevertheless, the conditions were excellent with very little cirrus and seeing $\approx 0\farcs5$. We were able to close the AO system control loops on the star with a frame rate of 30 Hz. With sufficient counts in each wavefront sensor subaperture, a stable lock was maintained for the duration of the observations.

We acquired a sequence of nine dithered images in the K' filter (central $\lambda = 2.12 \, \mu m$) using the NIRC2 medium camera (plate scale = 20 mas pix^{-1}). Each frame consisted of 6 co-adds with 10 s of integration time per co-add, totaling 9 minutes of on-source exposure time. The images were processed by removing hot pixels, subtracting the sky-background, and aligning and co-adding the cleaned frames. Figure 3 shows the contrast curve based on the AO image. The field of view is $9\farcs8 \times 9\farcs8$, which corresponds to 2.45 *Kepler* pixels on a
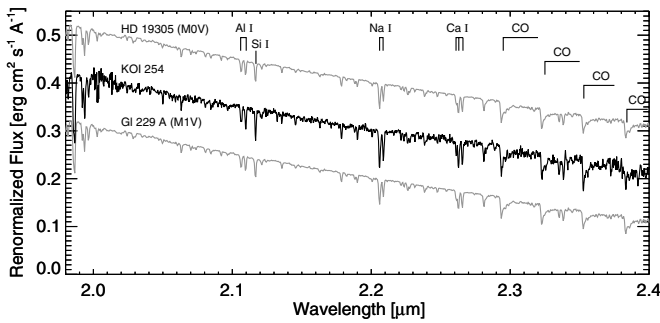
Figure 4. TripleSpec NIR spectra in *K* band for KOI-254 and two other early M dwarfs for comparison (HD 199305 [M0V] and Gl 229A [M1V]). The comparison spectra are taken from the Infrared Telescope Facility (IRTF) spectral library (gray; Cushing et al. 2005; Rayner et al. 2009). We also indicate strong atomic features identified by Cushing et al. (2005). The *K*-band Na I doublet and Ca I triplet have been shown to be sensitive to metallicity (Rojas-Ayala et al. 2010).

side. No obvious contaminants were identified in the immediate vicinity of KOI-254. Using the limits from our AO images, we are able to rule out any contaminating sources to a level of $\Delta K' = \{1.0, 3.2, 5.6, 6.9, 6.9\}$ at 3σ for separations of $\{0.''25, 0.''5, 1.''0, 2.''0, 4.''0\}$, respectively. The non-detection of nearby stars, together with the RV orbit presented in Section 2.3 clearly rule out blend scenarios and support the planetary interpretation of the transit signals.

2.5. Palomar Near-infrared Spectroscopy

We obtained near-infrared spectra of KOI-254 with the TripleSpec Spectrograph at the Palomar Observatory 200 inch Hale Telescope (Herter et al. 2008). The spectra were obtained as part of a survey of low-mass Kepler Objects of Interest described in Paper 1. TripleSpec is a cross-dispersed, long-slit, near-infrared spectrograph, dispersing a 1×30 arcsec slit from 1.0 to 2.5 μm across five orders at resolution $\lambda/\Delta\lambda = 2700$. Two positions on the slit, A and B, were used for each target, and exposures were taken in an ABBA pattern. Observations were taken on June 12, 13, and 18 of 2011. On June 12, the seeing was photometric, and three ABBA sets were taken with 30 exposures at each position. On June 13, seeing was 1.5–2 arcsec, and four ABBA sets were taken with 60 exposures at each position. On June 18, seeing was back to photometric, and four ABBA sets were taken with 60 s exposures.

Spectroscopic observations at near-infrared wavelengths must contend with telluric absorption lines introduced by Earth's atmosphere. Telluric lines vary strongly with air mass and humidity, and are calibrated by observing an object with a known spectrum at similar air mass and near in time to the science target observations. To calibrate the telluric lines in KOI-254 we observed HD 183204, an A0 star found using SIMBAD, which was within 0.1 air masses of KOI-254 at the times of the observations.

The spectra were extracted using a version of the SpexTool program modified for the Palomar TripleSpec Spectrograph (Cushing et al. 2004). The xtellcor package within SpeXTool accepts spectra of A0 stars and compares them to a model spectrum of Vega to identify and remove telluric absorption lines in a target spectrum (Vacca et al. 2003). Figure 4 plots the *K*-band spectrum of KOI-254 along with templates of similar spectra type (HD 199305 [M0V] and Gl 229A [M1V]), with the relevant spectral features indicated. We only show *J*, *H*, and *K* bands, as the regions between are heavily obscured by telluric

water vapor. The templates are taken from the SpeX library (Cushing et al. 2005; Rayner et al. 2009). The NIR spectrum of KOI-254 is consistent with an M0 dwarf.

3. ANALYSIS

3.1. Analysis of Broadband Photometry

The process of measuring the physical properties of stars generally involves comparing an observed temperature indicator (e.g., color) and luminosity (apparent magnitude, bolometric correction and parallax) to theoretical models of stellar evolution (e.g., Nordström et al. 2004; Valenti & Fischer 2005; Takeda et al. 2008). Such a comparison is typically performed through an interpolation of the observables onto a grid of models, and locating the combination of stellar properties that provide the closest match to the observations. However, the process is complicated for low-mass stars in general because of inaccuracies in theoretical evolution models (Torres 2007).

Fortunately, for ages $\gtrsim 100$ Myr and spectral types earlier than M5, M dwarfs reside very close to the zero-age main sequence, and at a fixed metallicity have a one-to-one mapping between mass and luminosity. Indeed, in the NIR *J*, *H*, and K_S bands, the mass–luminosity relationship is independent of metallicity (Allard et al. 1997; Delfosse et al. 2000). The metallicity dependence of the mass–luminosity relationship in optical bands provides a means of estimating stellar metallicities using broadband photometry (Bonfils et al. 2005; Johnson et al. 2009; Schlaufman & Laughlin 2010). Additional relationships have been discovered between optical–NIR colors and spectral type (West et al. 2005). These various relationships each provide leverage in the determination of the stellar properties, all without appealing to theoretical stellar structure and atmosphere models.

Our methodology is similar to the approach used by Johnson et al. (2011a) to measure the properties of low-mass *Kepler* target star, LHS 6343. In that case Johnson et al. took advantage of the common distance and composition of each component of the visual M+M binary system to solve for the mass and radius of the binary component transited by a brown dwarf. In the present work we generalize the methodology for single M dwarfs by enlarging the number of color and magnitude relationships included in the analysis, including a new NIR color-based metallicity calibration described in the Appendix.

We treat the stellar properties $\{a\} = \{M_\star, [\mathrm{Fe/H}], d\}$ as free parameters in a set of models that reproduce the observables $\{D\} = \{D_0, D_1, \ldots, D_{N-1}\}$, where $M_\star$ is the star's mass in solar units, $[\mathrm{Fe/H}]$ is the metallicity and d is the distance from the Sun measured in pc. The observed quantities $\{D\} = \{J, H, K_S, V, r - J, a_R, r - i\}$ are the apparent magnitudes, colors and transit parameters, with their associated measurement uncertainties $\{\sigma\}$.

Each observed quantity and its uncertainty are representative of a probability density function (pdf), approximated by a normal function with mean D_i and width σ_i, which can be evaluated at the value predicted by a model as a function of the parameters $\{a\}$. This calculation provides a probability of a datum conditioned on the model parameters, and the "best-fitting" values of the parameters are those that maximize the probability of the full set of observed data. For the case in which the pdf of each measurement is described adequately by a normal distribution, one recovers the special situation in which maximizing the probability of the data is equivalent to

minimizing χ^2, where

$$\chi^2 = \sum_{i=1}^{N_{\text{obs}}} \left[\frac{D_i - f_i(a)}{\sigma_i} \right]^2 + \sum_{j=1}^{N_{\text{par}}} |\ln p(a_j)|. \qquad (1)$$

In this expression, $f_i(a)$ is a model function that transforms the parameters $\{a\}$ into a prediction of an observation D_i. The $p(a_j)$ are probability terms that encode prior knowledge about the parameters $\{a\}$. For most of these we adopt normal distributions such that $|\ln p(a_j)| = (a_{\text{prior,j}} - a_j)^2 / \sigma_{a_j}^2$, where $a_{\text{prior,j}}$ is the most likely value of a_j based on prior knowledge, and σ_{a_j} is the width of the normal distribution centered on $a_{\text{prior,j}}$. These terms thus serve as "penalty functions" that increase χ^2 for deviations far from prior knowledge of the parameter values.

3.2. Relationship Between Apparent Magnitude and $\{M_\star, d\}$

Delfosse et al. (2000, hereafter D00) provide mass–luminosity relationships based on low-mass eclipsing binaries in the three 2MASS bands (J, H, K_S), with the tightest correlation between stellar mass and absolute K_S magnitude, M_{K_S}. Rather than computing a mass based on an absolute magnitude, which we lack due to an unknown parallax, we instead evaluate predictions of the apparent magnitude m_j for $j = \{J, H, K_S\}$ given a stellar mass $M_\star$, and distance d. This can be expressed as

$$m_j(M_\star, d) = \mathcal{M}_j(M_\star) + 5 \log_{10}(d/10) + A_j, \qquad (2)$$

where $\mathcal{M}_j(M_\star)$ are provided by J11 as polynomial expressions with coefficients listed in their Table 3, and A_j are extinction terms. We adopt a normally-distributed prior distribution for these terms based on $A_V = 0.195 \pm 0.02$ from the KIC. Further, we adopt the reddening law given for sight line to KOI-254 as listed in the NASA/IPAC Extragalactic Database based on Schlegel et al. (1998). However, we find that our results are unchanged if we adopt $A_V = 0$, indicating that extinction is minimal at the distance and direction of KOI-254.

3.3. Relationship Between Apparent Magnitude and $\{M_\star, [Fe/H], d\}$

The V-band magnitude can be related to the stellar mass and metallicity in a manner similar to the method used by J11, namely

$$V(M_\star, [Fe/H], d) = \mathcal{M}_V(M_\star, [Fe/H]) \\ + 5 \log_{10}(d/10) + A_V \qquad (3)$$

where

$$\mathcal{M}_V(M_\star, [Fe/H]) = \sum_{k=1}^{4} b_{V,k} [\mathcal{M}_{K_S}(M_\star) \\ + (0.71[Fe/H] - 0.091)]^k \qquad (4)$$

where the coefficients $\{b_V\}$ are given in Table 3 of J11. The second term in brackets, the linear function of [Fe/H], differs from that used by J11 owing to a revised broadband metallicity calibration that compares well with that of Schlaufman & Laughlin (2010).

An additional constraint on the metallicity is provided by our new $J - K_S$ metallicity calibration described in the Appendix and expressed in Equation (A3).

3.4. Relationship Between $a/R_\star$ and $M_\star$

The mass can also be estimated using the scaled semimajor axis from the fit to the transit light curve (e.g., Seager & Mallén-Ornelas 2003; Sozzetti et al. 2007; Winn 2008). The scaled semimajor axis, $a_R \equiv a/R_\star$ is related to the stellar density via Kepler's third law:

$$a_R(M_\star, P) = \left(\frac{G}{4\pi^2} \right)^{1/3} \frac{M_\star^{1/3}}{R_\star(M_\star)} P^{2/3}, \qquad (5)$$

where we have assumed $M_P \ll M_\star$. The function $R_\star(M_\star)$ relates the stellar mass to the radius, with both quantities in solar units. J11 used the empirical mass–radius relationship of Ribas (2006). However, the radii used in this analysis are based on short-period eclipsing binaries, for which there is the possibility that rotation-induced magnetic and coronal activity, as well as metallicity-inhibited convection may lead to anomalously inflated radii compared to single M dwarfs (López-Morales 2007; Kraus et al. 2011). In the present analysis, we use an empirical mass–radius relationship based on the interferometric radii of nearby M dwarfs measured by Boyajian et al. (2012), which gives a polynomial relationship that is very similar to the one used by J11 based on the eclipsing binaries in the Ribas (2006) sample.

3.5. Relationship Between $r - J$ Color and $M_\star$

Finally, to further constrain the mass of the star, we used the color–luminosity relationships of West et al. (2005). Specifically, we used columns 2, 5, and 6 from their Table 1 to relate $\mathcal{M}_J$ to $r - J$. We then recast the relationship in terms of stellar mass using $\mathcal{M}_J(M_\star)$ from J11 to give

$$(r - J)[M_\star] = 0.6587 \times \mathcal{M}_J(M_\star) - 1.738 + (A_r - A_J). \quad (6)$$

3.6. Joint Analysis of the Stellar Properties

We searched for the best-fitting values of the model parameters $\{a\}$ and their uncertainties using a Markov Chain Monte Carlo (MCMC) algorithm (see, e.g., Tegmark et al. 2004; Ford 2005; Winn et al. 2007; Johnson et al. 2011b). The MCMC technique uses the data and priors to explore the shape of the posterior pdf for each parameter of a model, conditioned on the available data. MCMC, particularly with the Metropolis–Hastings algorithm, provides an efficient means of exploring high-dimensional parameter space and mapping out the posterior pdf for each model parameter.

At each "chain link" in our MCMC analysis one parameter is selected at random and is altered by drawing a random variate from a transition probability distribution. In our case we use a normally distributed, pseudo-random number as the random variate. If the resulting value of the χ^2 for the trial parameters is greater than the previous value, then the set of trial parameters are accepted and added to the chain. If not, then the probability of adopting the new parameter set is $\exp(\Delta\chi^2)$, where $\Delta\chi^2$ is the difference in the fitting statistic from the previous and current steps. If the current trial is rejected then the parameters from the previous step are adopted. The width of the transition function determines the efficiency of convergence. If it is too narrow then the full exploration of parameter space is slow and the chain is susceptible local minima; if it is too broad then the chain exhibits large jumps and the acceptance rates are low.

The various empirical calibrations we use are not exact and have uncertainties owing to the imperfect calibration data used
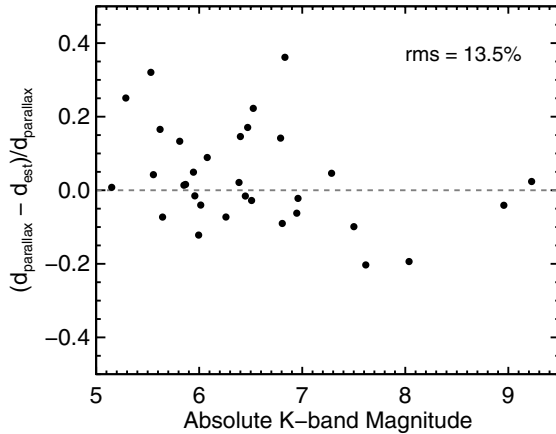
Figure 5. Fractional difference between known parallax-based distances of nearby M dwarfs, d_{parallax}, and estimated distances from our broadband photometric method, d_{est}. The differences are plotted vs. the absolute K_S-band magnitude $\mathcal{M}_{K_S}$. The rms indicates that our method has a precision of 13.5%, which is consistent with the 68.2% confidence region from our MCMC analysis of KOI-254.

to construct them. For example, we refitted the Delfosse et al. mass–luminosity relationship using their calibration stars and found an rms scatter in the absolute magnitudes about the best-fitting polynomial relationships. For example, we find that the rms scatter in M_{K_S} from the Delfosse et al. calibration stars is 0.18 mag. We adopt this as our uncertainty in K_S for KOI-254 in place of the value reported in second column of Table 1. Our adopted NIR uncertainties are given in column 3 of Table 1.

We tested our methodology on a sample of nearby M dwarfs with well-measured parallaxes from van Leeuwen (2007), 2MASS photometry and SDSS r magnitudes from the Carlesberg Meridian Catalog (CMC14; Evans et al. 2002). For our test we treated each of these stars as though their distances, and $\mathcal{M}_{K_S}$ values were unknown, and used the available photometry in our MCMC scheme to estimate their distances. The results are shown in Figure 5. The fractional, rms of our mass estimates about the D00 values is 13.5%, which we adopt as our measurement uncertainty.

3.7. Stellar Properties Measured From Photometry

We find a stellar mass $M_\star = 0.59 \pm 0.06\,M_\odot$ and a stellar radius $R_\star = 0.55 \pm 0.11\,R_\odot$, where the value in parentheses is the systematic error in our distance estimates based on the rms scatter shown in Figure 5. We also find [Fe/H] $= +0.13 \pm 0.13$ and $d = 333 \pm 50$ pc. The 68.2% confidence region for our MCMC estimate of the distance is consistent with the 13.5% rms scatter seen in Figure 5. This is an indication that our inflated measurement errors on our photometric measurements are estimated properly and account for the systematic errors in the empirical calibrations we employ in our analysis. Figure 6 shows the two-dimensional posterior probability distributions for our stellar parameters.

3.8. Analysis of NIR Spectra

The moderate-resolution K-band spectra of late-type stars contain atomic lines highly sensitive to metallicity and continuum regions sensitive to effective temperature (Covey et al. 2010; Rojas-Ayala et al. 2010). We use the spectral indices and calibrations of Rojas-Ayala et al. (2012) to measure the iron abundance [Fe/H], overall metallicity [M/H], and effective temperature T_{eff} of KOI-254. The metallicity and effective temperature relations use the equivalent widths of the Ca I triplet
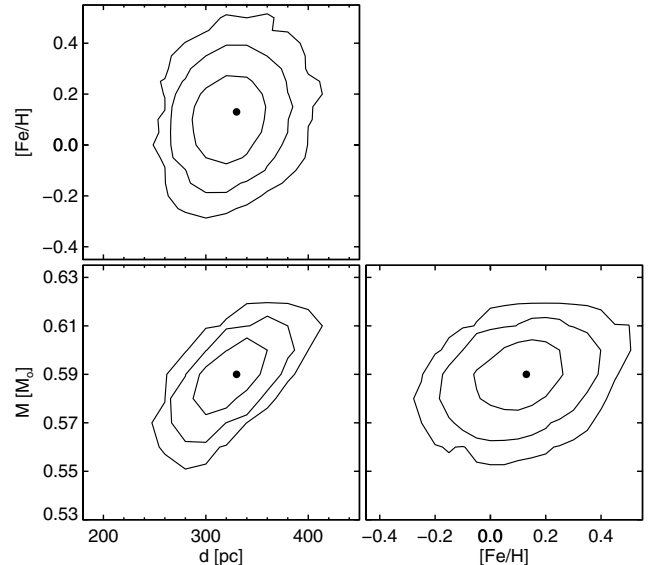
Figure 6. Each panel shows the joint, posterior pdfs for two stellar parameters at a time, marginalized over the remaining parameters. The contours show the isoprobability levels corresponding to {68.2, 95, 99.7}% confidence. The best-fitting values are shown as solid circles.

and Na I doublet in K-band and the H_2O-K2 index: a measurement of the deformation of the K-band pseudo-continuum using regions dominated by water absorption (based on the H_2O-K of Covey et al. 2010). The metallicity relations are empirically calibrated using M dwarfs with wide F-, G-, or K-type companions, which have metallicity measurements in the SPOCS catalog (Valenti & Fischer 2005). The effective temperatures are measured by interpolating the H_2O-K2 value and the measured overall metallicity [M/H] of a given star onto a grid of H_2O-K2, [M/H], and T_{eff} calculated using the BT-Settl-2010 model spectral spectra of Allard et al. (2010). The grid consists of BT-Setl-2010 spectra for effective temperatures between 2200 and 4000 K with 100 K increments, and [M/H] values of -1.0, -0.5, 0.0, $+0.3$, and $+0.5$. The H_2O-K2 is calculated from the model spectra, providing a well-sampled grid of H_2O-K2, [M/H], and T_{eff} values.

We use Monte Carlo simulations to calculate the measurement uncertainties of the [Fe/H], [M/H], and T_{eff} values. We calculate the values for 1000 realizations of the spectra, each with noise added based on the per-channel error estimates reported by SpeXTool. We take the standard deviation in the resultant distribution of [Fe/H], [M/H] and T_{eff} as the measurement uncertainty in those values. Rojas-Ayala et al. (2012) estimate a systematic uncertainty of 0.14 for [Fe/H] and 0.10 for [M/H] for the metallicity relations. For the T_{eff}, we estimate a systematic uncertainty of 50 K.

Using these methods, and combining the measurement and systematic uncertainties in quadrature, we measure [Fe/H] $+0.28 \pm 0.14$, [M/H] $= +0.20 \pm 0.10$ and $T_{\mathrm{eff}} = 3815 \pm 88$ K for KOI-254 using the K-band analysis. Similar parameters appear in Paper 1, which uses the same data. The parameters are consistent with the results from the photometric analysis within the estimated uncertainties.

4. LIGHT CURVE ANALYSIS

4.1. Joint Analysis and Planet Properties

We simultaneously analyzed a total of 49 *Kepler* transit light curves, a single *Z*-band light curve from the Nickel telescope
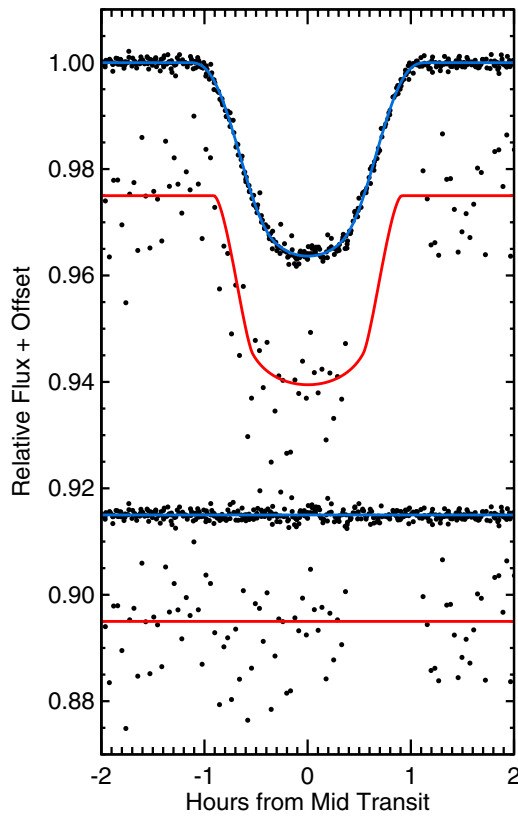
Figure 7. *Kepler* (upper, blue) and Nickel (lower, red) light curves, phased at the photometric period. The Nickel light curve has been offset artificially for clarity. The best-fitting light curve models are shown for each data set (see Section 4), and the residuals are shown beneath each light curve.

(A color version of this figure is available in the online journal.)

at Lick Observatory, and our 14 RV observations acquired with Keck/HIRES. The Nickel and HIRES observation timestamps were converted to BJD$_{UTC}$ to match *Kepler* MAST data using the techniques of Eastman et al. (2010).

We fitted the *Kepler* and Nickel light curves using version 3.01 of the Transit Analysis Package (Gazak et al. 2011), which uses the analytic eclipse model of Mandel & Agol (2002). For the *Kepler* transits we resampled the model to a cadence of 60 s before rebinning to the 29.4 minute observing cadence to account for long integration light curve distortions (Kipping 2010). We determined the best-fitting parameters and their uncertainties using the same Metropolis–Hastings implementation described in Section 3, with which we employ a Daubechies fourth-order wavelet decomposition likelihood function (Carter & Winn 2009). Wavelet decomposition techniques provide increased confidence in derived MCMC uncertainties over the traditional χ^2 likelihood by allowing parameters which measure photometric scatter (uncorrelated Gaussian σ_w, and $1/f$ correlated red σ_r) to evolve as free parameters. The technique recovers the χ^2 likelihood in the case where $\sigma_r = 0$ and σ_w is locked at a value characteristic to the observed data. For the RV data we fitted a Keplerian model using the partially linearized scheme of Wright & Howard (2009).

Of the fifteen parameters in this technique, thirteen vary freely within our MCMC analysis: the period P, Inclination i, the scaled semimajor axis a_R, the radius ratio R_p/R_s, times of mid-transit T_{tr}, eccentricity e, argument of periastron ω, σ_w, σ_r, RV amplitude K, the systemic velocity offset γ, and two parameters to account for global linear trends in the data normalization.

Table 3
KOI-254 Transit Mid-times and Ephemeris Residuals

T_{mid} (BJD-2450000.0)	T_{mid}−Ephemeris	Telescope
54964.5368 ± 0.0015	−0.00048 ± 0.0018	K
54966.99228 ± 0.00081	−0.00024 ± 0.0013	K
54969.44698 ± 0.00084	−0.00076 ± 0.0013	K
54971.90303 ± 0.00092	0.000059 ± 0.0014	K
54974.35835 ± 0.00095	0.00015 ± 0.0014	K
54976.81357 ± 0.00092	0.00014 ± 0.0014	K
54979.26833 ± 0.00083	−0.00033 ± 0.0013	K
54981.72302 ± 0.00096	−0.00087 ± 0.0014	K
54984.17923 ± 0.00086	0.00011 ± 0.0013	K
54986.6343 ± 0.0015	−0.000025 ± 0.0018	K
54989.08909 ± 0.00091	−0.00049 ± 0.0014	K
54991.54493 ± 0.00068	0.00012 ± 0.0012	K
54993.9996 ± 0.0010	−0.00043 ± 0.0014	K
54996.45456 ± 0.00096	−0.00070 ± 0.0014	K
55003.8211 ± 0.0010	0.00015 ± 0.0014	K
55006.27645 ± 0.00085	0.00027 ± 0.0013	K
55008.73088 ± 0.00085	−0.00054 ± 0.0013	K
55011.18647 ± 0.00081	−0.00017 ± 0.0013	K
55013.6420 ± 0.0010	0.00012 ± 0.0014	K
55018.55210 ± 0.00098	−0.00023 ± 0.0014	K
55021.0084 ± 0.0010	0.00088 ± 0.0014	K
55023.46242 ± 0.00084	−0.00036 ± 0.0013	K
55025.91715 ± 0.00073	−0.00087 ± 0.0012	K
55028.37311 ± 0.00091	−0.00014 ± 0.0013	K
55030.82892 ± 0.00083	0.00044 ± 0.0013	K
55033.2832 ± 0.0020	−0.00051 ± 0.0022	K
55035.7396 ± 0.0011	0.00069 ± 0.0015	K
55038.19468 ± 0.00084	0.00052 ± 0.0013	K
55040.64897 ± 0.00062	−0.00042 ± 0.0012	K
55043.10475 ± 0.00085	0.00013 ± 0.0013	K
55045.55956 ± 0.00091	−0.00029 ± 0.0014	K
55048.01603 ± 0.00081	0.00095 ± 0.0013	K
55050.47094 ± 0.00093	0.00063 ± 0.0014	K
55052.92573 ± 0.00088	0.00020 ± 0.0013	K
55055.3827 ± 0.0011	0.0019 ± 0.0015	K
55057.83570 ± 0.00070	−0.00030 ± 0.0012	K
55060.29115 ± 0.00093	−0.000073 ± 0.0014	K
55062.74626 ± 0.00089	−0.00019 ± 0.0013	K
55065.20262 ± 0.00087	0.00094 ± 0.0013	K
55067.65679 ± 0.00091	−0.00012 ± 0.0014	K
55070.11231 ± 0.00071	0.00017 ± 0.0012	K
55072.56725 ± 0.00085	−0.00012 ± 0.0013	K
55075.02311 ± 0.00089	0.00051 ± 0.0013	K
55077.47754 ± 0.00097	−0.00029 ± 0.0014	K
55079.9343 ± 0.0010	0.0012 ± 0.0014	K
55082.38913 ± 0.00094	0.00084 ± 0.0014	K
55084.84365 ± 0.00086	0.00013 ± 0.0013	K
55087.29916 ± 0.00084	0.00041 ± 0.0013	K
55089.75411 ± 0.00099	0.00014 ± 0.0014	K
55742.84449 ± 0.0027	−0.00047 ± 0.0029	N

Note. K—Kepler, N—Nickel Z-band.

The remaining two limb-darkening coefficients evolve under normal priors. For the Nickel Z-band data we adopted from Claret (2004): $\mu_1 = 0.353 \pm 0.35, \mu_2 = 0.255 \pm 0.025$. For the *Kepler* data we used the coefficients listed by Sing (2010): $\mu_1 = 0.521 \pm 0.056$, and $\mu_2 = 0.225 \pm 0.052$. It is important to note that our joint fitting procedure allowed uncertainties in the orbital eccentricity to propagate into the determination of the Keplerian orbit parameters and the scaled semimajor axis a_R.

We ran 40 independent MCMC chains each with 5×10^5 links for a total of 1.4×10^7 total inference links after removing

Table 4
System Parameters for KOI-254

Parameter	Value	68.3% Confidence Interval	Comment
Transit Parameters			
Orbital period, P (days)	2.455239	± 0.000004	A
Radius ratio, $(R_P/R_\star)$	0.179	± 0.002	A
Transit depth, $(R_P/R_\star)^2$	0.03204	± 0.00072	A
Scaled semimajor axis, $a/R_\star$	10.6	± 1	A
Orbit inclination, i (deg)	87.0	± 0.7	A
Transit impact parameter, b	0.6	± 0.2	A
Rotation period, $P_{\rm rot}$ (days)	15.8	± 0.2	A
Other Orbital Parameters			
Eccentricity	0.11	$^{+0.1}_{-0.09}$	A, C
Argument of periastron ω (deg)	230	± 68	C
Velocity semiamplitude $K_\star$ (m s^{-1})	110	± 10	C
Stellar Parameters			
$M_\star$ ($M_\odot$)	0.59	± 0.06	D
$R_\star$ ($R_\odot$)	0.55	± 0.11	D
$\rho_\star$ [$\rho_\odot$]	4	± 2	A
$\log g_\star$ (cgs)	4.7	± 0.2	B
[Fe/H]	$+0.13$	± 0.13	D
[Fe/H]$_{\rm NIR}$	$+0.28$	± 0.14	F
[M/H]$_{\rm NIR}$	$+0.20$	± 0.10	F
Distance (pc)	333	± 33	D
$T_{\rm eff,NIR}$ (K)	3820	± 90	G
Planet Parameters			
M_P [$M_{\rm Jup}$]	0.505	± 0.090	B,C
R_P [$R_{\rm Jup}$]	0.96	± 0.11	B
Mean planet density, ρ_p (g cm^{-3})	0.8	± 0.5	B,C
$\log g_P$ (cgs)	3.1	± 0.1	A
Equilibrium temperature $T_{\rm eff}(R_*/a)^{1/2}$ (K)	1000	± 20	D

Notes. (A) Determined from the light curves. (B) Based on group A parameters supplemented by the photometric stellar mass determination described in Section 3. (C) Based on our analysis of the Keck/HIRES RV measurements. (D) Based on our photometric mass and radius determinations described in Section 3.3. (E) Based on photometric metallicity calibrations described in Section 3 and the Appendix. (F) Based on the analysis of our TripleSpec NIR spectra using the methodology of Rojas-Ayala et al. (2012).

the burn-in portion of the chains. We test for and find good convergence using the Gelman–Rubin statistic (Gelman & Rubin 1992). For the *Kepler* light curves we find typical values of $\sigma_w = 0.00049$ and $\sigma_r = 0.0018$. For the Nickel light curve we find $\sigma_w = 0.0064$ and $\sigma_r = 0.024$.

Based on our light curve analysis, together with the stellar properties in Section 3.7, we measure a planetary mass of $M_P = 0.505 \pm 0.090\ M_{\rm Jup}$, and a radius $R_P = 0.96 \pm 0.19\ R_{\rm Jup}$. The complete list of stellar and planet parameters and their uncertainties is given in Table 4.

We also tested for achromatic transit depths, δ, by fitting the *Kepler* and Nickel light curves separately. We found $\delta_{\rm Kepler} = 0.179 \pm 0.002$ and $\delta_{\rm Nickel} = 0.183 \pm 0.016$.

4.2. Searching for Transit Timing Variations

To measure the individual transit mid-times we fixed all of the global parameters ($R_P/R_\star$, $a/R_\star$, P, i and the limb-darkening coefficients) and fitted each transit event separately using the MCMC algorithm described in Section 4. Table 3 lists the time at the mid-point of each transit $T_{\rm mid}$; the difference between the measured values and those predicted by a linear ephemeris; and the formal measurement uncertainties, which are typically of order 2 minutes. We see no statistically significant timing variations.

4.3. Limits on the System Age

Measuring the ages of M-type stars is notoriously difficult, except for the rare cases when stars are in clusters or associations, or show indications of extreme youth. One way of estimating the age of late-type field stars is gyrochronology (Barnes 2010). Using this idea, age-period calibrations have been produced for G and K type dwarfs, (Mamajek & Hillenbrand 2008), but relationships for M dwarfs are still uncertain.

The 122 day *Kepler* light curve shows clear evidence of rotational modulation, with seven complete cycles shown in Figure 1. From these data we estimate a rotational period of 15.8 ± 0.2 days for KOI-254. This period can be directly compared with the rotational period sequence of the Hyades cluster (Delorme et al. 2011). From their Figure 15, and using our estimate of $V - K = 4.0 \pm 0.1$ for KOI 254, it can be seen that stars in the 625 Myr Hyades cluster (Perryman et al. 1998) with equivalent colors are rotating with a comparable average period of 14 days. This suggests that the system is relatively young, similar in age to the Hyades.

We have generated a more detailed estimate of KOI-254's age using the gyrochronology relations derived by Barnes (2010). These relations express a star's current day rotation period as a function of its convective turnover timescale and rotation period on the ZAMS. To calibrate our estimate, we adopted

the relationship between a star's mass and convective turnover time as tabulated by Barnes & Kim (2010), and calculated three age estimates assuming the ZAMS rotation periods required to reproduce the spread of rotation rates observed for $\approx 0.6\,M_\odot$ stars in the 600 Myr Praesepe open cluster (Agüeros et al. 2011). Assuming a ZAMS rotation period of 2.81 days, as required to reproduce the median rotation period for $0.6\,M_\odot$ Praesepe members, the Barnes (2010) gyrochrone relations predict an age of ≈ 780 Myr from the 15.8 day rotation period of KOI-254. However, a considerable range of periods are observed for Praesepe members in the mass range: adopting the ZAMS rotation periods required to reproduce the 10th and 90th percentile rotation periods observed for $0.6\,M_\odot$ stars in Praesepe indicates that KOI-254's age could plausibly be as low as 380 Myr or as old as 1.5 Gyr.

This estimate relies on the assumption that the rotational evolution of KOI 254 hasn't been grossly affected by tidal effects due to its hot Jupiter (e.g., Lanza 2010). From its measured proper motion of 20.9 ± 3.2 mas yr^{-1} (Monet et al. 2003) and our derived distance of 333 ± 33 pc, the system's tangential velocity is a moderate 34 ± 6 km s^{-1}. While deriving kinematic ages for individual star systems is unreliable, the space motion of KOI-254 indicates that it's age is consistent with 0.5 Gyr.

5. SUMMARY AND DISCUSSION

We report the detection of a short-period, Jupiter-mass planet that transits an early M-type dwarf star. The host star has mass $M_\star = 0.59\,M_\odot$ and a radius $R_\star = 0.55\,R_\odot$, which we measure using a new method that draws upon broadband optical and NIR photometry, together with various empirical calibrations of M dwarf properties. Using our estimated stellar parameters, we find that the planet has a period of 2.455239 days, a mass $M_P = 0.505\,M_{\rm Jup}$, and a radius $R_P = 0.96\,R_{\rm Jup}$. At the planet's semimajor axis of 0.030 AU and given the star's estimated effective temperature of $T_{\rm eff} = 3680$ K, the planet has an equilibrium temperature of 1000 K (see Table 4 for the full list of parameters and uncertainties).

Based on the rotation of the KOI-254, we estimate an age of roughly 0.5 Gyr. Examination of the tabulated theoretical planetary radii computed by Fortney et al. (2007) for an age of 0.3 Gyr and stellar insolation equal to that of KOI-254 b shows that our measured planet radius is consistent with model expectations, but only for a core mass of $\approx 50\,M_\oplus$. For the 1 Gyr models a $25\,M_\oplus$ core is necessary to reproduce the observed radius. This is a remarkably large core mass (heavy element content) and conforms well with the observed correlation between planetary heavy element content and host star metallicity (Burrows et al. 2007; Torres et al. 2008; Miller & Fortney 2011). This in turn agrees with observations to date that suggest that the formation of a Jupiter-mass planet around a low-mass star requires high metallicity (Johnson & Apps 2009; Schlaufman & Laughlin 2010; Rojas-Ayala et al. 2010).

As a Jupiter-mass planet with a period less than 10 days, KOI-254 b is the sole example of a hot Jupiter orbiting an M dwarf. More than 300 stars have been monitored in various RV surveys and a planet with $P < 30$ days has not been found around an M-type dwarf, despite the large expected Doppler signal. Indeed, a planet such as KOI-254 b would be readily detectable in any of the past and present M dwarf Doppler surveys conducted over the past 15 years (see e.g., Endl et al. 2003; Johnson et al. 2010b; Bonfils et al. 2011). Given the difficulties associated with photometrically monitoring a large sample of M dwarfs, and the paucity of giant planets around
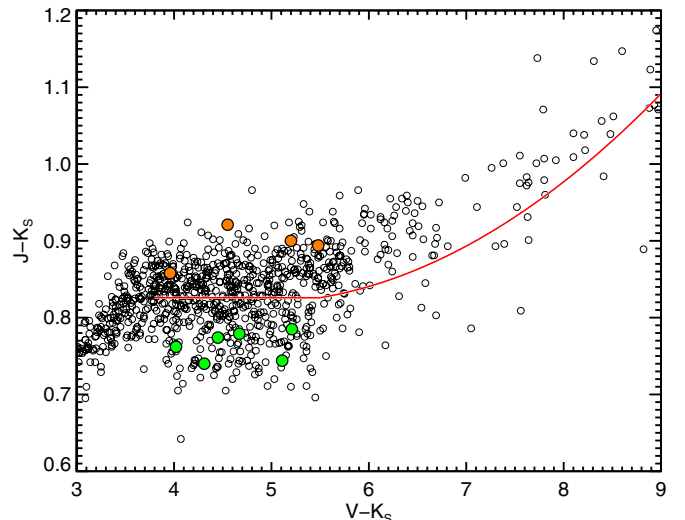
Figure 8. Color–color diagram for low-mass stars in the solar neighborhood. The "main sequence" is approximated by a constant for $V - K < 5.5$, and a polynomial for redder values (solid line). Metal-rich M dwarfs known to have [Fe/H] > +0.25 as based on their FGK dwarf companions are highlighted above the main sequence (orange circles). Metal-poor stars with [Fe/H] < -0.25 are shown below the main sequence (green circles), indicating a relationship between metallicity and the distance a star lies away from the main sequence.

(A color version of this figure is available in the online journal.)

low-mass stars, this fortuitous *Kepler* detection may serve as our lone example of a hot Jupiter around an M dwarf for some time to come.

APPENDIX

A NEW COLOR-BASED METALLICITY CALIBRATION

Inspection of the locations of low-mass dwarfs in the $(J - K)$–$(V - K)$ color–color diagram reveals a dramatic increase in the width of the main sequence beyond $V - K \approx 4$, corresponding to the onset of strong molecular band heads characteristic of the M spectral type (Figure 8). Several M dwarfs known to be metal-rich based on the [Fe/H] of their more massive binary companions lie along the upper envelope of the scatter in $J - K$. Similarly, several known metal-poor dwarfs reside in the lower portion of the diagram, suggesting that the increased scatter in $J - K$ color is due to the effects of metallicity.
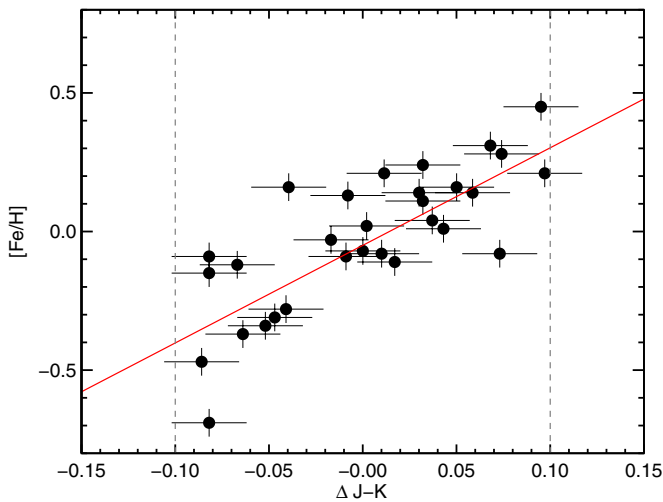
Figure 9. Metallicity of our calibration stars plotted against the distance of a star from the isometallicity contour shown in Figure 8, parameterized by $\Delta(J-K) \equiv (J-K)_{\mathrm{meas}} - (J-K)_0$. The linear relationship (red solid line) is given by Equation (A2). The dashed lines denote the $\Delta(J-K)$ limits between which our calibration is valid, roughly corresponding to $-0.5 < [\mathrm{Fe/H}] < +0.5$.
(A color version of this figure is available in the online journal.)

This color–metallicity effect has been noted previously by Leggett (1992) and Lépine & Shara (2005). The reason for the effect is most likely due to changes in continuous opacities due to molecular species such as H_2^-, H^-, He^-, H_2^+, and C^- (Allard & Hauschildt 1995). Additionally, sources of line opacity can be seen in the spectral standards compiled by Rayner et al. (2009). The J-band (≈ 1.2–$1.35\,\mu$m) spectra of M dwarfs exhibit deep potassium (K) and iron hydride (FeH) absorption features, along with dozens of shallower metal lines such as Na, Mg, Fe, and Si. On the other hand, the K_S-band (≈ 2.1–$2.35\,\mu$m) is relatively featureless, with a few relatively shallow Na and Ca lines as the only prominent absorption features. Thus, higher stellar metallicity preferentially suppresses J-band flux, causing the star's $J-K$ color to become redder.

To calibrate the relationship between $J-K$ color and metallicity, we first fitted a two-part function to the color–color diagram shown in Figure 8. This main sequence is approximated well by a constant $(J-K)_0 = 0.835$ for $3.8 \leqslant V-K < 5.5$. For $V-K \geqslant 5.5$ we fitted a polynomial $(J-K)_0 = \sum_i a_i (V-K)^i$ where $\{a\} = \{1.637, -0.2910, 0.02557\}$. We assume the main sequence in this color–color plane is an isometallicity contour with a value equal to the mean [Fe/H] of the solar neighborhood. Based on an 18-pc volume-limited sample of stars in the Spectroscopic Properties of Cool Stars catalog (Valenti & Fischer 2005), Johnson & Apps (2009) measure a mean metallicity of [Fe/H] -0.05.

Next, we follow the methodology of Bonfils et al. (2005) and use a calibration sample of M dwarfs with widely separated, FGK-type, common-proper-motion companions. The metallicity of the M-type companion in each pair is assumed to be the same as that of the more massive companion, for which spectroscopic parameters can be estimated accurately. We gathered our collection of 30 calibration stars from the SPOCS catalog and elsewhere in the literature.

Figure 9 shows the metallicity of our calibration stars plotted against $\Delta(J-K) \equiv (J-K)_{\mathrm{meas}} - (J-K)_0$. We fitted a linear relationship holding the offset fixed such that [Fe/H] $= -0.05$

at $\Delta(J-K) = 0$, and found an acceptable fit of the form

$$[\mathrm{Fe/H}] = -0.050 + 3.520\Delta(J-K)$$
$$= 2.872 + 3.520(J-K)\,[\,\pm 0.15\ \mathrm{dex}]\quad (A1)$$

$$\text{valid for } -0.1 < \Delta(J-K) < 0.1. \quad (A2)$$

The residuals to our fit have a rms $= 0.15$ dex, which we adopt as the measurement uncertainty. It is important to note that our calibration sample only spans $-0.1 < \Delta(J-K) < +0.1$, corresponding to $-0.5 < [\mathrm{Fe/H}] < +0.5$.

We incorporate this calibration along with several other constraints in the analysis presented in Section 3 to provide a jointly constrained calibration for stellar mass, metallicity and distance. To be consistent with our joint analysis, it is necessary to invert Equation (A2) to give

$$(J-K) = 0.816 + 0.284[\mathrm{Fe/H}]. \quad (A3)$$

It is important to note that this simplified version of Equation (A2) is only valid for our specific analysis of KOI-254, which has $V-K < 5.5$.

REFERENCES

Agüeros, M. A., Covey, K. R., Lemonias, J. J., et al. 2011, ApJ, 740, 110
Albrecht, S., Winn, J. N., Johnson, J. A., et al. 2011, ApJ, 738, 50
Allard, F., & Hauschildt, P. H. 1995, ApJ, 445, 433
Allard, F., Hauschildt, P. H., Alexander, D. R., & Starrfield, S. 1997, ARA&A, 35, 137
Allard, F., Homeier, D., & Freytag, B. 2010, arXiv:1011.5405
Barnes, S. A. 2010, ApJ, 722, 222
Barnes, S. A., & Kim, Y.-C. 2010, ApJ, 721, 675
Batalha, N. M., Borucki, W. J., Koch, D. G., et al. 2010, ApJ, 713, L109
Bonfils, X., Delfosse, X., Udry, S., et al. 2005, A&A, 442, 635
Bonfils, X., Gillon, M., Forveille, T., et al. 2011, A&A, 528, A111
Borucki, W. J., Koch, D. G., Basri, G., et al. 2011, ApJ, 728, 117
Boyajian, T. S., McAlister, H. A., van Belle, G., et al. 2012, ApJ, 746, 101
Brown, T. M., Latham, D. W., Everett, M. E., & Esquerdo, G. A. 2011, AJ, 142, 112
Burrows, A., Hubeny, I., Budaj, J., & Hubbard, W. B. 2007, ApJ, 661, 502
Butler, R. P., Marcy, G. W., Williams, E., et al. 1996, PASP, 108, 500
Butler, R. P., Vogt, S. S., Marcy, G. W., et al. 2004, ApJ, 617, 580
Carter, J. A., & Winn, J. N. 2009, ApJ, 704, 51
Charbonneau, D., Berta, Z. K., Irwin, J., et al. 2009, Nature, 462, 891
Charbonneau, D., Brown, T. M., Burrows, A., & Laughlin, G. 2007, in Protostars and Planets, ed. V. B. Reipurth, D. Jewitt, & K. Keil (Tucson, AZ: Univ. Arizona Press), 701
Claret, A. 2004, A&A, 428, 1001
Covey, K. R., Lada, C. J., Román-Zúñiga, C., et al. 2010, ApJ, 722, 971
Crossfield, I. J. M., Hansen, B. M. S., Harrington, J., et al. 2010, ApJ, 723, 1436
Cushing, M. C., Rayner, J. T., & Vacca, W. D. 2005, ApJ, 623, 1115
Cushing, M. C., Vacca, W. D., & Rayner, J. T. 2004, PASP, 116, 362
Delfosse, X., Forveille, T., Ségransan, D., et al. 2000, A&A, 364, 217
Delorme, P., Collier Cameron, A., Hebb, L., et al. 2011, MNRAS, 413, 2218
Eastman, J., Siverd, R., & Gaudi, B. S. 2010, PASP, 122, 935
Endl, M., Cochran, W. D., Tull, R. G., & MacQueen, P. J. 2003, AJ, 126, 3099
Evans, D. W., Irwin, M. J., & Helmer, L. 2002, A&A, 395, 347
Ford, E. B. 2005, AJ, 129, 1706
Fortney, J. J., Marley, M. S., & Barnes, J. W. 2007, ApJ, 659, 1661
Gazak, J. Z., Johnson, J. A., Tonry, J., et al. 2011, arXiv:1102.1036
Gelman, A., & Rubin, D. B. 1992, Stat. Sci., 7, 457
Gillon, M., Pont, F., Demory, B.-O., et al. 2007, A&A, 472, L13
Herter, T. L., Henderson, C. P., Wilson, J. C., et al. 2008, Proc. SPIE, 7014, 70140X
Howard, A. W., Johnson, J. A., Marcy, G. W., et al. 2010, ApJ, 721, 1467
Ida, S., & Lin, D. N. C. 2005, ApJ, 626, 1045
Irwin, J., Buchhave, L., Berta, Z. K., et al. 2010, ApJ, 718, 1353
Johnson, J. A., Aller, K. M., Howard, A. W., & Crepp, J. R. 2010a, PASP, 122, 905

Johnson, J. A., & Apps, K. 2009, ApJ, 699, 933
Johnson, J. A., Apps, K., Gazak, J. Z., et al. 2011a, ApJ, 730, 79
Johnson, J. A., Butler, R. P., Marcy, G. W., et al. 2007, ApJ, 670, 833
Johnson, J. A., Clanton, C., Howard, A. W., et al. 2011b, ApJS, 197, 26
Johnson, J. A., Howard, A. W., Marcy, G. W., et al. 2010b, PASP, 122, 149
Johnson, J. A., Marcy, G. W., Fischer, D. A., et al. 2006, ApJ, 647, 600
Johnson, J. A., Winn, J. N., Cabrera, N. E., & Carter, J. A. 2009, ApJ, 692, L100
Johnson, J. A., Winn, J. N., Narita, N., et al. 2008, ApJ, 686, 649
Kennedy, G. M., & Kenyon, S. J. 2008, ApJ, 673, 502
Kipping, D. M. 2010, MNRAS, 408, 1758
Knutson, H. A., Charbonneau, D., Burrows, A., O'Donovan, F. T., & Mandushev, G. 2009, ApJ, 691, 866
Kraus, A. L., Tucker, R. A., Thompson, M. I., Craine, E. R., & Hillenbrand, L. A. 2011, ApJ, 728, 48
Lanza, A. F. 2010, A&A, 512, A77
Laughlin, G., Bodenheimer, P., & Adams, F. C. 2004, ApJ, 612, L73
Leggett, S. K. 1992, ApJS, 82, 351
Lépine, S., & Shara, M. M. 2005, AJ, 129, 1483
López-Morales, M. 2007, ApJ, 660, 732
Madhusudhan, N., & Seager, S. 2011, ApJ, 729, 41
Mamajek, E. E., & Hillenbrand, L. A. 2008, ApJ, 687, 1264
Mandel, K., & Agol, E. 2002, ApJ, 580, L171
Marcy, G., Butler, R. P., Fischer, D., et al. 2005, Prog. Theor. Phys. Suppl., 158, 24
Miller, N., & Fortney, J. J. 2011, ApJ, 736, L29
Monet, D. G., Levine, S. E., Canzian, B., et al. 2003, AJ, 125, 984
Morton, T. D., & Johnson, J. A. 2011, ApJ, 738, 170
Muirhead, P. S., Hamren, K., Schlawin, E., et al. 2011, arXiv:1109.1819

Nordström, B., Mayor, M., Andersen, J., et al. 2004, A&A, 418, 989
Perryman, M. A. C., Brown, A. G. A., Lebreton, Y., et al. 1998, A&A, 331, 81
Rayner, J. T., Cushing, M. C., & Vacca, W. D. 2009, ApJS, 185, 289
Ribas, I. 2006, Ap&SS, 304, 89
Rojas-Ayala, B., Covey, K. R., Muirhead, P. S., & Lloyd, J. P. 2010, ApJ, 720, L113
Rojas-Ayala, B., Covey, K. R., Muirhead, P. S., & Lloyd, J. P. 2012, ApJ, 748, 93
Schlaufman, K. C., & Laughlin, G. 2010, A&A, 519, A105
Schlegel, D. J., Finkbeiner, D. P., & Davis, M. 1998, ApJ, 500, 525
Seager, S., & Mallén-Ornelas, G. 2003, ApJ, 585, 1038
Sing, D. K. 2010, A&A, 510, A21
Skrutskie, M. F., Cutri, R. M., Stiening, R., et al. 2006, AJ, 131, 1163
Sozzetti, A., Torres, G., Charbonneau, D., et al. 2007, ApJ, 664, 1190
Takeda, Y., Sato, B., & Murata, D. 2008, PASJ, 60, 781
Tegmark, M., Strauss, M. A., Blanton, M. R., et al. 2004, Phys. Rev. D, 69, 103501
Torres, G. 2007, ApJ, 654, 1095
Torres, G., Winn, J. N., & Holman, M. J. 2008, ApJ, 677, 1324
Vacca, W. D., Cushing, M. C., & Rayner, J. T. 2003, PASP, 115, 389
Valenti, J. A., & Fischer, D. A. 2005, ApJS, 159, 141
van Leeuwen, F. 2007, A&A, 474, 653
West, A. A., Walkowicz, L. M., & Hawley, S. L. 2005, PASP, 117, 706
Winn, J. N. 2008, in ASP Conf. Ser. 398, Extreme Solar Systems, ed. D. Fischer, F. A. Rasio, S. E. Thorsett, & A. Wolszczan (San Francisco, CA: ASP), 101
Winn, J. N., Holman, M. J., & Fuentes, C. I. 2007, AJ, 133, 11
Wright, J. T., & Howard, A. W. 2009, ApJS, 182, 205